

Entropic Stabilization and Retrograde Solubility in Zn_4Sb_3

Gregory S. Pomrehn¹, Eric S. Toberer¹, G. Jeffrey Snyder^{1,*} and Axel van de Walle^{1†}

¹ - *Materials Science, California Institute of Technology,
1200 E. California Blvd., Pasadena, California 91125, USA*

(Dated: February 24, 2024)

Zn_4Sb_3 is shown to be entropically stabilized versus decomposition to Zn and ZnSb though the effects of configurational disorder and phonon free energy. Single phase stability is predicted for a range of compositions and temperatures. Retrograde solubility of Zn is predicted on the two-phase boundary region between Zn_4Sb_3 and Zn. The complex temperature dependent solubility can be used to explain the variety of nanoparticle formation observed in the system: formation of ZnSb on the Sb rich side, Zn on the far Zn rich side and nano-void formation due to Zn precipitates being reabsorbed at lower temperatures.

PACS numbers: 65.40.gd, 64.70.qd, 63.20.-e, 84.60.Rb, 81.30.Bx

Keywords: Zn_4Sb_3 Phase Stability

A. Introduction

The Zn-Sb binary phase system has been of interest for many years in the search for efficient and low-cost thermoelectric materials. Of primary interest has been the Zn_4Sb_3 phase which exhibits a thermoelectric figure of merit, zT , in excess of 1 in intermediate temperature ranges¹. This phase, being composed of environmentally benign and relatively earth abundant elements, continues to draw active research.

Zn_4Sb_3 exhibits exceptionally low lattice thermal conductivity¹, due in part to its high configurational disorder. The room temperature structure of Zn_4Sb_3 ($R\bar{3}c$, Figure 1), denoted ' $\beta\text{-Zn}_4\text{Sb}_3$ ' here¹ (or sometimes ' $\epsilon\text{-Zn}_4\text{Sb}_3$ '²), contains an anionic framework composed of 30 Sb, divided between 6 Sb_2^{4-} dimers and 18 isolated Sb^{3-} . With 39 Zn^{2+} a charge balanced composition is obtained at $\text{Zn}_{13}\text{Sb}_{10}$. Of these Zn cations, at most, 36 can fit on Zn framework sites and 3 must be distributed among 3 crystallographically distinct interstitial sites³. For clarity, we will always refer to the entire phase as ' Zn_4Sb_3 ' and write ' $\text{Zn}_X\text{Sb}_{10}$ ' only when referring to a specific configurational composition within ' Zn_4Sb_3 '.

Previous ab initio studies of Zn_4Sb_3 have included the electronic density of states and formation energy of various atomic configurations ranging in composition from $\text{Zn}_{12}\text{Sb}_{10}$ to $\text{Zn}_{14}\text{Sb}_{10}$ ⁴⁻⁷. These results confirm the expectation from charge counting that $\text{Zn}_{13}\text{Sb}_{10}$ has a Fermi level in the band gap, Zn-deficient $\text{Zn}_{12}\text{Sb}_{10}$ has a Fermi level in the valence band and Zn-rich $\text{Zn}_{14}\text{Sb}_{10}$ has a Fermi level in the conduction band. All reports of formation energy⁵⁻⁷ also show agreement that all Zn_4Sb_3 configurations have a positive formation enthalpy at 0K with respect to Zn and ZnSb. Yet Zn_4Sb_3 is observed below 700K. Furthermore, at low temperature, a reversible transition to a low symmetry, meta-stable, ordered ' α ' (and α') phase is observed^{8,9}.

Synthetically, Zn_4Sb_3 is usually prepared with excess Zn: $\text{Zn}_{13.3}\text{Sb}_{10}$. As Zn has a high vapor pressure even at the relatively low synthesis and operation temperature, as well as the tendency to readily oxidize¹⁰, it is

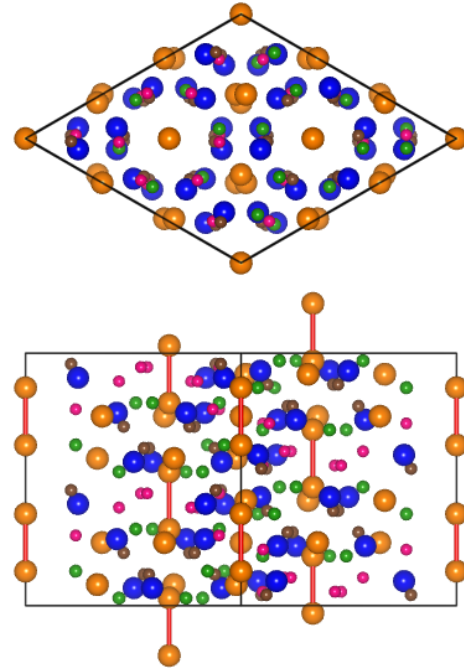


FIG. 1: (Color online) Conventional hexagonal unit cell of Zn_4Sb_3 . The Sb sub-lattice (orange) is composed of isolated Sb and Sb dimers. The Zn 'A' sub-lattice (blue) is 90% occupied. The 'B' (green), 'C' (brown), and 'D' (pink) Zn sub-lattices are 5% occupied. The primitive rhombohedral cell is 1/3 the volume of the conventional cell.

not very surprising that excess Zn helps form the phase. Zn_4Sb_3 is always a heavily doped p-type semiconductor with room temperature (Hall) carrier concentration between $6 - 9 \times 10^{19}/\text{cm}^3$.¹¹ According to the simple charge counting and ab initio calculations, this would be best explained by a slight Zn deficiency, $\text{Zn}_{13-\delta}\text{Sb}_{10}$, where δ should be between 0.016 and 0.024. If n/n_{Hall} is 2 as predicted by Singh⁴, then δ should be between 0.008 and 0.012. It is perhaps surprising that with all the interstitial Zn sites, synthesis with excess Zn does not produce

n-type material.

In this work, we expand on previous ab initio results to consider a thorough thermodynamic investigation of Zn_4Sb_3 . A thermodynamic ensemble approach is necessary because no single configuration (or even small number of configurations) can adequately describe the phase. By assembling a Grand Canonical Partition Function we are able to quantitatively prove entropic stabilization. We also predict a region of single phase stability on a temperature versus composition diagram that exhibits retrograde solubility of Zn with $\delta > 0$ that would always produce p-type Zn_4Sb_3 in intermediate temperatures.

B. Computational Methods

The natural thermodynamic function to account for a range of possible compositions is the Grand Canonical Potential¹² (GCP):

$$\phi(T, \mu) = -\frac{k_B T}{N} \ln \left(\sum_s e^{-(E_s - \mu \cdot N_s)/k_B T} \right) \quad (1)$$

where k is Boltzmann's constant, T is temperature, N is the total number of atoms in the system, E_s is the total energy of state s , N_s is a vector of the number of atoms in each species in state s (with elements summing to N) and μ is a vector containing the chemical potential of each species. This greatly simplifies for both Zn and ZnSb, which do not exhibit configurational disorder:

$$\phi(T, \mu) = \frac{\varepsilon_0}{n} - \mu \cdot x_0 \quad (2)$$

where ε_0 is the energy per unit cell, n is the number of atoms per unit cell and x_0 is the composition in atomic fraction.

For Zn_4Sb_3 , we consider the GCP within an independent cells approximation. We assume that each primitive unit cell of 23 ± 2 atoms is non-interacting with neighboring cells, in the sense that the defect configuration present in one cell does not affect the energies of defect configurations in a nearby cell. (All our ab initio calculations are nevertheless performed on infinite periodic systems with suitable k-point sampling.) This approach is useful in this system because the unit cell is rather large. This assumption is validated by computing the energy of supercells with different configurations in each primitive unit cell and comparing it to that predicted by summing the energies of the constituent primitive cells. Under the independent cells approximation:

$$\phi(T, \mu) = \frac{\varepsilon_0}{n} - \mu \cdot x_0 - \frac{k_B T}{n} \ln \left(1 + \sum_{i>0} m_i e^{-(\Delta\varepsilon_i - \mu \cdot \Delta n_i)/k_B T} \right) \quad (3)$$

where ε_0 is the ground state energy per unit cell, n is the number of atoms per unit cell and x_0 is the ground

state composition. For each configuration, i , m_i is the symmetric multiplicity, $\Delta\varepsilon_i$ is the change in energy from the ground state and Δn_i is the change in the number of atoms from the ground state.

The energy for each configuration is calculated under the generalized gradient approximation (GGA) using the projector augmented wave (PAW) method with Perdew-Burke-Ernzerhof (PBE) potentials as implemented in VASP 4.6, neglecting spin orbit coupling. All unit cell parameters and atomic positions were allowed to relax to find the lowest energy configuration to within 10^{-4} eV. A final static calculation was performed for an accurate total energy.

Defect configurations were systematically generated by enumerating defect combinations deviating from the undefected $\text{Zn}_{12}\text{Sb}_{10}$ structure ('A' sub-lattice fully occupied and 'B', 'C' and 'D' sub-lattices fully unoccupied). Defect clusters were composed of a combination of vacancies on the 'A' sub-lattice, and occupation of an interstitial site on the 'B', 'C' or 'D' sub-lattices. Clusters of up to 6 defects were enumerated, excluding some structures because the defects were too close (nearest neighbor A and C sites both occupied). After allowing the atomic configuration to relax, the resulting atomic positions were projected onto the closest unrelaxed configuration and any duplicate configurations were excluded in order to avoid over-counting states.

Phonon density of states and vibrational free energies were calculated using the 'supercell' method as implemented in the Alloy Theoretic Automated Toolkit (ATAT)¹³⁻¹⁵. Since the computational resources needed to compute phonon modes for all Zn_4Sb_3 configurations are prohibitive, representative configurations were selected at four compositions between $\text{Zn}_{12}\text{Sb}_{10}$ and $\text{Zn}_{15}\text{Sb}_{10}$ configurations. A second $\text{Zn}_{13}\text{Sb}_{10}$ configuration was computed as well to assess the error in our approximation. For each of these configurations and the end-members Zn and ZnSb, phonon modes were calculated at 0%, 1% and 2% strain to account for the effects of thermal expansion, under the quasi-harmonic approximation.

The vibrational contribution to the free energy is incorporated into the GCP through a nested sum in the partition function¹⁶. For each distinct configuration, phonon occupation accounts for small displacements around the local energy minimum, resulting in a temperature dependent free energy correction.

GCPs were assembled for Zn, Zn_4Sb_3 and ZnSb. Phase equilibrium is determined by equality of two respective GCPs. The equilibrium composition of each phase can be determined by:

$$\nabla_\mu \phi(T, \mu) = -x \quad (4)$$

C. Results and Discussion

Over 100 unique, stable configurations were enumerated in the β - Zn_4Sb_3 primitive rhombohedral unit cell

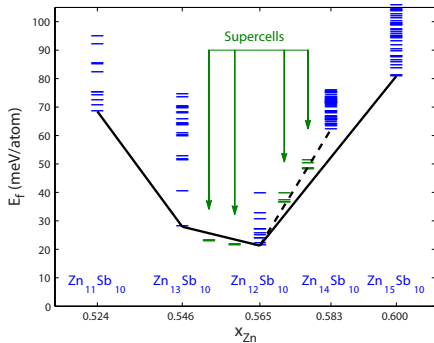


FIG. 2: (Color online) Formation enthalpy at 0K for Zn_4Sb_3 configurations with respect to Zn and ZnSb . The solid black line represents the convex hull of structures confined to the Zn_4Sb_3 lattice. Supercell calculations in green were done using the conventional unit cell, each composed of three primitive unit cells. The dashed line shows the predicted energy for supercells following the independent cells approximation.

with between 21 and 25 atoms per cell (the number of Sb was held constant at 10). The 0K formation enthalpy of these configurations with respect to Zn and ZnSb is shown in Figure 2.

Consistent with previous theoretical studies^{5–7}, all configurations have a positive formation enthalpy with respect to Zn and ZnSb . The convex hull is plotted in solid black and connects the ground state configurations (for Zn_4Sb_3 phase) at each composition. The composition $\text{Zn}_{14}\text{Sb}_{10}$ does not have a configuration touching the convex hull. This means that for an ensemble of atoms of composition $\text{Zn}_{14}\text{Sb}_{10}$ constrained to remain in the Zn_4Sb_3 lattice, it would be more energetically favorable to form a mixture of cells of composition $\text{Zn}_{13}\text{Sb}_{10}$ and $\text{Zn}_{15}\text{Sb}_{10}$. If the system is allowed to adopt any lattice, then, at 0K, it would be even more energetically favorable to separate into Zn and ZnSb crystals. Figure 2 also allows us to test the independent cells approximation. The data points marked supercells are all made up of 3 primitive cells of different compositions to yield the intermediate compositions shown. Between $\text{Zn}_{12}\text{Sb}_{10}$ and $\text{Zn}_{13}\text{Sb}_{10}$, we see that the supercells produce a slightly lower energy by about 3 meV/atom than predicted by the independent cells approximation. Between $\text{Zn}_{13}\text{Sb}_{10}$ and $\text{Zn}_{14}\text{Sb}_{10}$, the energies from the supercells are either very close or slightly higher than predicted by the independent cells approximation (the dashed line). The small energy difference of a few meV/atom justifies the use of the independent cells approximation, although a consideration of a possible systematic error is discussed later.

The formation free energy due to phonons (relative to Zn and ZnSb) is shown in Figure 3 for the 5 representative configurations. In all cases, the phonon contribution to the free energy favors the Zn_4Sb_3 phase over Zn and ZnSb . This is likely a result of the softer phonon modes in the more complex and open crystal structure. Increasing Zn concentration and thereby increasing the Zn-disorder

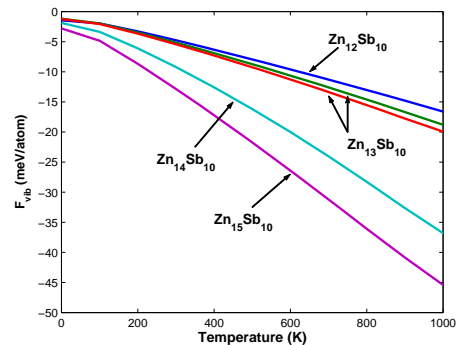


FIG. 3: Phonon contribution to the formation free energy with respect to Zn and ZnSb . The two $\text{Zn}_{13}\text{Sb}_{10}$ configurations are in good agreement to 1 meV/atom. There is a more favorable contribution to the formation energy for more disordered Zn-rich configurations.

results in a more favorable contribution to the free energy. There is good agreement between the two configurations of composition $\text{Zn}_{13}\text{Sb}_{10}$, differing by 1 meV/atom at 1000K. It then seems reasonable to assume that the vibrational free energy of the representative structures may be applied to all the configurations at that composition when we compute the GCP of Zn_4Sb_3 .

The computed region of single phase stability for Zn_4Sb_3 is shown in Figure 4. Including configurational and vibrational effects to the free energy, Zn_4Sb_3 is found to stabilize at around 700K at a composition of $\text{Zn}_{12.992}\text{Sb}_{10}$. As the temperature increases, the range of stable single phase compositions increases, more broadly on the Zn deficient side. (Eventually, the solid melts, but our analysis focuses on the solid-state portion of the phase diagram.) Interestingly, on the Zn-rich side, we observe retrograde solubility of Zn. That is, the highest stable concentration of Zn in Zn_4Sb_3 decreases with increasing temperature. This unusual finding is a result of the composition-dependent relationship between the enthalpy and entropy of mixing. Typically defects of all kinds entropically stabilize stoichiometric variations on both sides of a valence precise composition. In the case of Zn_4Sb_3 , the valence precise composition is already ‘defected’ with interstitial Zn. A miscibility gap arises for compositions above $\text{Zn}_{13}\text{Sb}_{10}$ due to the large jump in formation enthalpy compared to the Zn-deficient compositions. The effect is lessened by the counteractive effects of higher vibrational entropy for the Zn-rich compositions. If the vibrational effects were neglected, the Zn-rich boundary would not curve to the right until a much higher temperature.

The region of single phase stability shown in Figure 4 has readily observable consequences. The black vertical line at composition $\text{Zn}_{13}\text{Sb}_{10}$ represents the valence precise structure with a Fermi level inside the band gap. At any Zn-deficient composition from $\text{Zn}_{13}\text{Sb}_{10}$, we expect a partially filled valence band resulting in a p-type

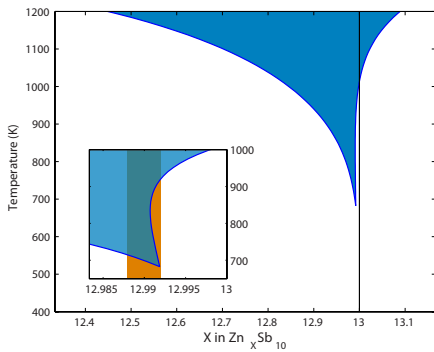


FIG. 4: (Color online) Single phase stability region for Zn_4Sb_3 . Solid black line corresponds to the charge balanced composition. Stable compositions to the left of the line will result in a p-type semiconductor. Inset shows a close-up of the region of retrograde Zn solubility. The orange band corresponds to compositions estimated from charge carrier measurements¹¹.

semiconductor. (Surprisingly, there is a recent report of a $\text{Zn}_{13}\text{Sb}_{10}$ configuration being slightly p-type¹⁷. Our electronic density of states results are in agreement with previous studies⁴⁻⁷.) All stable compositions below 1000K in Figure 4 result in a p-type semi-conductor. Attempting to dope Zn_4Sb_3 with excess Zn will not result in an n-type semiconductor but a two-phase equilibrium between Zn metal and p-type Zn_4Sb_3 . Furthermore, with the consideration of retrograde solubility, if Zn-saturated single phase Zn_4Sb_3 is heated up, it passes through a region where it becomes thermodynamically more stable to precipitate Zn metal. With more heating, the Zn is re-absorbed as more Zn-rich compositions are stable. Upon cooling, the same precipitation and absorption should occur if held in thermodynamic equilibrium.

On the Zn-deficient side of the stable phase region the usual temperature dependent solubility is observed. Here one would expect ZnSb to precipitate as the temperature is reduced. Because this would occur at low temperature in the solid state, small nanometer sized precipitates would be expected. Such particles are indeed observed in Sb-rich samples¹¹.

The high temperature phase boundary on the Zn-rich side could explain the formation of Zn nanoparticles observed in some Zn_4Sb_3 samples¹⁸. Cooling a Zn-rich composition above $\text{Zn}_{13}\text{Sb}_{10}$ would precipitate Zn (possibly nano-particles if cooled fast enough¹⁹). Upon further cooling through the retrograde region, some of the Zn would be reabsorbed into the β -phase. The absorption of nanoparticle Zn may explain the nano-voids observed in some samples¹¹.

Experimental carrier concentration measurements from Toberer¹¹ from single phase β - Zn_4Sb_3 samples range from $6 - 9 \times 10^{19}/\text{cm}^3$. This corresponds to a composition range of 0.002% atomic Zn between $\text{Zn}_{12.988}\text{Sb}_{10}$ and $\text{Zn}_{12.992}\text{Sb}_{10}$ assuming $n/n_{\text{Hall}} = 2$.⁴ This concentration range, corresponding to the orange band in the

inset of Figure 4, is in close agreement with the predicted stable compositions near the stabilization temperature. This composition range is much smaller than the 0.2% atomic Zn observed by microprobe analysis. This discrepancy is not surprising since the composition range is basically the limit of the microprobe resolution.

There is some expected uncertainty in our predicted temperature of stabilization of Zn_4Sb_3 . Our predicted temperature of 700K is much higher than might be expected. There are several possible explanations for this. One could be a deficiency in our methodology to fully account for the sources of entropy in such a complex disordered structure. Our enumeration method may underestimate the number of Zn_4Sb_3 configurations by comparing the relaxed structures to the fixed lattice in Figure 1, which represents, in a sense, a measured average over many possible configurations. The vibrational contribution to the free energy has a significant effect in lowering the stabilization temperature. Assuming a representative structure for each composition might be an underestimate for the more disordered configurations and the effect could be even more pronounced. Lastly, we noted earlier that the supercells on the Zn-deficient side of $\text{Zn}_{13}\text{Sb}_{10}$ had slightly lower formation energy than expected under the independent cells approximation. This neglected cell-to-cell interaction (2 meV/atom) could lower the stabilization temperature by several hundred degrees. In either case, we expect the retrograde solubility to remain, and possibly intensify, because the supercells on the Zn-rich side of $\text{Zn}_{13}\text{Sb}_{10}$ are in good agreement with the independent cells approximation.

To ensure that our finding of a single-phase region for the β - Zn_4Sb_3 lattice is not an artifact of the independent cell approximation, we have conducted separate Monte Carlo simulations based on a cluster expansion Hamiltonian fitted to our database of structural energies. These simulations confirm the presence of a single phase region over the temperature range where β - Zn_4Sb_3 is stable. Hence, the independent cell approximation was deemed reliable and was used throughout this work. It provides a convenient explicit expression for the free energy and is immune to the fitting errors inherent to the Hamiltonian construction procedure.

Finally, we consider how Zn_4Sb_3 might interact with other nearby phases, namely, α - Zn_4Sb_3 and Zn_8Sb_7 . First principles calculation of α - Zn_4Sb_3 yields positive formation energy of 19 meV/atom with respect to Zn and ZnSb . This is 3 meV/atom below the lowest energy β - Zn_4Sb_3 configuration of composition $\text{Zn}_{13}\text{Sb}_{10}$. Assuming no configurational disorder in α - Zn_4Sb_3 we predict β - Zn_4Sb_3 to become energetically favorable compared to α - Zn_4Sb_3 at 300K (although both are still meta-stable with respect to Zn and ZnSb at this temperature). It seems possible that there is a temperature range in which meta-stable β - Zn_4Sb_3 is observed before becoming thermodynamically stable with respect to Zn and ZnSb at some higher temperature.

Another phase of recent interest is Zn_8Sb_7 , which has

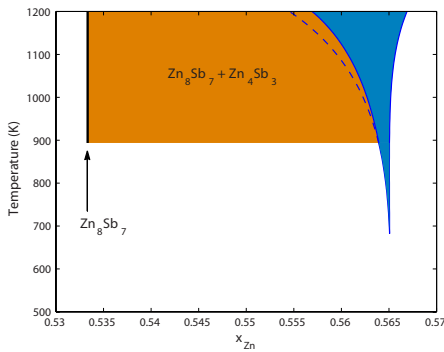


FIG. 5: (Color online) Possible phase stability regions of Zn_4Sb_3 and Zn_8Sb_7 under conditions favorable to the formation of Zn_8Sb_7 . The dotted line represents the phase boundary of Zn_4Sb_3 in the absence of Zn_8Sb_7 .

been characterized experimentally and studied through first principles calculations^{20,21}. These calculations reveal that, even though Zn_8Sb_7 is unstable in bulk form, it could be stabilized in nanocrystalline form if surface stress or energy contributions result in a free energy decrease of 5 meV/atom (relative to ZnSb and Zn_4Sb_3). Taking these assumptions into effect, the resulting phase diagram is shown in Figure 5. We see that Zn_8Sb_7 would stabilize at a temperature higher than Zn_4Sb_3 and a two phase region results. This also reduces the stable Zn-deficient Zn_4Sb_3 composition range predicted in the ab-

sence of Zn_8Sb_7 (dashed line in Figure 5). Other unidentified phases as reported in some phase diagrams²² could have a similar effect.

D. Conclusions

From our first principles investigation, we have shown that Zn_4Sb_3 is entropically stabilized with the help of configurational and vibrational entropy. Under the independent cells approximation of the grand canonical potential we predict a region of single phase stability near $\text{Zn}_{12.992}\text{Sb}_{10}$, which results in a nominally p-type semi-conductor. Additionally, we predict a temperature range with retrograde Zn solubility. The temperature dependent solubility can be used to explain the variety of nanoparticle formation observed in the system: formation of ZnSb on the Sb-rich side, Zn on the far Zn-rich side and nano-void formation due to Zn precipitates being reabsorbed at lower temperatures.

Acknowledgements

This work is supported by the U.S. National Science Foundation via grant DMR-0953378 and via TerraGrid resources at NCSA and SDSC under Grant No. TG-DMR050013N. The authors also thank the Caltech MURI project and DARPA.

-
- * jsnyder@caltech.edu
 † avdw@caltech.edu
- ¹ T. Caillat, J.-P. Fleurial, and A. Borshchevsky, *Journal of Physics and Chemistry of Solids* **58**, 1119 (1997).
 - ² G. Nakamoto *et al.*, *J Alloys Compd.* **432**, 116 (2007).
 - ³ G. Snyder, M. Christensen, E. Nishibori, T. Caillat, and B. Iversen, *Nature Mater.* **3**, 458 (2004).
 - ⁴ S.-G. Kim, I. I. Mazin, and D. J. Singh, *Phys. Rev. B* **57**, 6199 (1998).
 - ⁵ F. Cargnoni *et al.*, *Chemistry A European Journal* **10**, 3861 (2004).
 - ⁶ E. S. Toberer *et al.*, *Phys. Stat. Sol. RRL* **1**, 253 (2007).
 - ⁷ A. S. Mikhaylushkin, J. Nylen, and U. Haussermann, *Chemistry A European Journal* **11**, 4912 (2005).
 - ⁸ J. Nylen, M. Andersson, S. Lidin, and U. Haussermann, *Journal of the American Chemical Society* **126**, 16306 (2004), <http://pubs.acs.org/doi/pdf/10.1021/ja044980p>, PMID: 15600316.
 - ⁹ J. Nylen *et al.*, *Chemistry of Materials* **19**, 834 (2007), <http://pubs.acs.org/doi/pdf/10.1021/cm062384j>.
 - ¹⁰ H. Yin *et al.*, *Journal of Electronic Materials* **39**, 1957 (2010), 10.1007/s11664-009-1053-3.
 - ¹¹ E. S. Toberer, P. Rauwel, S. Gariel, J. Taftø, and G. Jeffrey Snyder, *J. Mater. Chem.*, (2010).
 - ¹² A. van de Walle and M. Asta, *Modelling Simul. Mater. Sci. Eng.* **10**, 521 (2002).
 - ¹³ A. van de Walle, M. Asta, and G. Ceder, *CALPHAD Journal* **26**, 539 (2002).
 - ¹⁴ A. van de Walle, *Calphad Journal* **33**, 266 (2009).
 - ¹⁵ A. van de Walle and G. Ceder, *Journal of Phase Equilibria* **23**, 348 (2002).
 - ¹⁶ A. van de Walle and G. Ceder, *Rev. Mod. Phys.* **74**, 11 (2002).
 - ¹⁷ A. N. Qiu, L. T. Zhang, and J. S. Wu, *Phys. Rev. B* **81**, 035203 (2010).
 - ¹⁸ . Prytz *et al.*, *Philosophical Magazine Letters* **89**, 362 (2009).
 - ¹⁹ T. Ikeda, V. A. Ravi, and G. J. Snyder, *Acta Materialia* **57**, 666 (2009).
 - ²⁰ C. S. Birkel *et al.*, *Journal of the American Chemical Society* **132**, 9881 (2010), <http://pubs.acs.org/doi/pdf/10.1021/ja1035122>.
 - ²¹ G. Pomrehn, unpublished work (2010).
 - ²² V. Izard, M. Record, and J. Tedenac, *J. Alloys Compd.* **345**, 257 (2002).